RSC Advances

ROYAL SOCIETY OF CHEMISTRY

PAPER

View Article Online
View Journal | View Issue

Check for updates

Cite this: *RSC Adv.*, 2020, **10**, 33718

DFT study of α-Keggin, lacunary Keggin, and iron$^{II–VI}$ substituted Keggin polyoxometalates: the effect of oxidation state and axial ligand on geometry, electronic structures and oxygen transfer†

Soheila Mir, Bahram Yadollahi, * Reza Omidyan and Gholamhasan Azimi

Received 12th June 2020
Accepted 3rd September 2020

DOI: 10.1039/d0ra05189f

rsc.li/rsc-advances

Herein, the geometry, electronic structure, Fe–ligand bonding nature and simulated IR spectrum of α-Keggin, lacunary Keggin, iron(II/III)-substituted and the important oxidized high-valent iron derivatives of Keggin type polyoxometalates have been studied using the density functional theory (DFT/OPTX-PBE) method and natural bond orbital (NBO) analysis. The effects of different Fe oxidation states (II–VI) and $H_2O/OH^-/O^{2-}$ ligand interactions have been addressed concerning their geometry and electronic structures. It has been revealed that the d-atomic orbitals of Fe and 2p orbitals of polyoxometalate's oxygen-atoms contribute in ligand binding. Compared with other high valent species, the considered polyoxometalate system of $[PW_{11}O_{39}(Fe^VO)]^{4-}$, possesses a high reactivity for oxygen transfer.

1. Introduction

Polyoxometalates (POMs) represent a diverse class of inorganic metal-oxide anion clusters with defined structures based on MO_6 octahedra mostly containing tungsten and/or molybdenum in their highest oxidation states.[1–3] Owing to their attractive structure along with chemical and electronic versatility, they have found different applications in catalysis, medicine and materials sciences.[4–6] Among a wide variety of heteropoly compounds, Keggin type POMs, $[XM_{12}O_{40}]^{n-}$, are the most stable and available species. Substitution of addenda atoms (W or Mo) in Keggins with other transition metals generates transition metal substituted Keggin type POMs (TMSPOMs). This type of substitution, as one of the main source of diversity, improves redox and acid/base properties of POMs in a variety of chemical processes.[2] Some of the TMSPOMs, such as high-valent iron–oxo species in heme enzymes (or metalloporphyrin complexes)[7,8] and nonheme reagents,[9] are used as oxidation catalyst in different organic reactions.

Understanding the effect of various properties, such as the roles of transition metals, framework metal atoms M_{FM}, and type of heteroatom X and counter ions, in TMSPOMs stability and reactivity could be useful in designing efficient POM-based materials in emerging technologies. Electronic structure and reactivity of this growing class of inorganic compounds need to comprehensive experimental and theoretical investigations.

As stated above, POMs and especially TMSPOMs have been used extensively in different catalytic oxidation reactions using environmentally friendly oxidants such as hydrogen peroxide. These compounds and some of their derivatives, which could be produced in the reaction medium, with respect to stability, energy and their properties, possibly will contribute in catalytic processes.

The structural and reactivity differences in high-valent metal derivatives of TMSPOMs allow the researchers to resort the computational examinations in this field. There are a vast number of reports devoted on theoretical exploration of POMs with focus on understanding the electronic structure, redox property, magnetism, and reaction mechanisms.[10–27] For example, the essential role of $[(X^{n+}O_4)M^{III}{}_2(OH)_2(M_{FW})_{10}O_{32}]^{(8-n)-}$ chemical composition – where M = Fe, Mn, Ru, M_{FW} = Mo and W, and X = Al^{III}, Si^{IV}, P^V, and S^{VI} – in the geometry, electronic structure, magnetic properties and defining lower-lying electronic state of these species were investigated. This, in turn, would possibly have an impact on their reactivity.[28,29] The molecular geometry, electronic structure, redox properties and metal-functional group bonding nature of a series of transition metal nitrido and dinitrogen derivatives of Keggin type POMs were also analyzed by density functional theory (DFT) and natural bond orbital (NBO) analysis. Their findings indicate that the electrophilic/nucleophilic reactivity and interaction between metal and functional group in these POMs is directly related to the transition metal substitution.[30–32] The systematic DFT and NBO analysis were employed to investigate the electronic structures and bonding features of the ruthenium(II)

Department of Chemistry, University of Isfahan, Isfahan 81746-73441, Iran. E-mail: yadollahi@chem.ui.ac.ir; yadollahi.b@gmail.com

† Electronic supplementary information (ESI) available. See DOI: 10.1039/d0ra05189f

atom and SO_2 molecule in the two ruthenium–sulfur dioxide (SO_2) adducts of *trans*-$Ru(NH_3)_4(SO_2)Cl^+$ and $[(SiW_{11}O_{39})Ru^{II}(SO_2)]$.[6–33] The DFT method has also been employed to design a new $[Mo_5O_{18}Fe{=}O]^{3-}$ catalyst, which would act as selective C–H hydroxylation reagent[34] and adopted to identify the electronic and redox properties, protonation, and stability of five $[\alpha\text{-}PTi_2W_{10}O_{40}]^{7-}$ isomers.[35] All of these valuable studies shed more light on the application of POMs in different realms.

The theoretical study of TMSPOMs derivatives is difficult because of multiple lower lying electronic states, high negative charges and large sizes. In this study, high level density functional theoretical method has been applied to study a Keggin POM, $\alpha\text{-}[PW_{12}O_{40}]^{3-}$ (PW_{12}), lacunary Keggin POM, $[PW_{11}O_{39}]^{7-}$ (PW_{11}), $Fe^{II/III}$ substituted Keggin POMs, $[PW_{11}O_{39}(Fe^{n+})]^{(7-n)-}$ ($PWFe^{n+}$) ($n = 2, 3$), $Fe^{II/III/IV}$ substituted Keggin POMs with H_2O ligand, $[PW_{11}O_{39}(Fe^{n+}OH_2)]^{(7-n)-}$ ($PWFe^{n+}OH_2$) ($n = 2, 3, 4$), and other high valent $Fe^{IV/V/VI}$ POMs with OH^- and O^{2-} ligands as potential active POM species. The significance of the work could be unravelled when the difficulties associated with theoretical studies of organometallic, owing to strong spin contamination problems would be taken into account. Fortunately, recent development in deMon2K code,[36] by implementing the auxiliary DFT approaches and robust algorithms made it feasible to study such heavy systems.

2. Results and discussion

2.1. Ground state geometries, charge distribution, electronic structure, and simulated infrared spectra of PW_{12} and PW_{11} anions

The most common Keggin heteropoly anions like PW_{12}, $[SiW_{12}O_{40}]^{4-}$ and $[PMo_{12}O_{40}]^{3-}$ are formed from simple oxoanions and required heteroatoms through a self-assembly process upon acidification in aqueous solutions.

$$12WO_4^{2-} + HPO_4^{2-} + 23H^+ \rightarrow [PW_{12}O_{40}]^{3-} + 12H_2O$$

Adding controlled amounts of hydroxide ions to the aqueous solution of these heteropoly anions could generate the lacunary (defect) POMs. These POM anions encompass one or more vacancies due to loss of addenda atom(s) from the structure. At the pH = 2, this process is expressed as follows:[37,38]

$$[PW_{12}O_{40}]^{3-} \rightleftarrows [PW_{11}O_{39}]^{7-} + WO^{4+}$$

The mono lacunary Keggin POMs could act as pentadentate ligands and so frequently applied in preparing TMSPOMs. These compounds come in a big variety and are used as acid or oxidation catalysts.

In this study, attempts are made to investigate the geometry, electronic structure and simulation of IR spectra of the mentioned POMs. The process begins with study on PW_{12} and followed by PW_{11}, where one WO^{4+} unit is removed, Fe substituted PW_{11} as $PWFe^{n+}$ (n = 2 and 3) and ended by $PWFe^{n+}OH_2$ (n = 2 and 3) with H_2O as the axial ligand. Since this TMSPOMs could be used as catalyst in oxidation reactions through the interaction between oxidant and catalyst, different types of high oxidation state Fe substituted Keggin POMs along with various axial ligands have been considered.

2.1.1. Ground state geometries. To compare with X-ray crystallography information for PW_{12} system,[21,35] the geometry optimization of PW_{12} and PW_{11} species have been performed in singlet, triplet and quintet spin states at DFT/OPTX-PBE/DZVP-GGA level (ESI†). Selected optimized geometry-parameters for PW_{12} and PW_{11} in singlet spin state are tabulated in Table 1. According to Table 1, the theoretical geometry parameters are in good agreement with the corresponding experimental values, while discrepancy appear only in the P–O_a bonds, which is underestimated by a 0.033 Å.

Bond length is a good parameter for evaluation of interaction strength between two atoms. By removing a WO^{4+} moiety from PW_{12}, the system's charge is varied from −3 to −7 in PW_{11}. As a result, the P^1–$O_a{}^{13}$ (1.597 Å), W^6–$O_a{}^{13}$ (2.516 Å), W^6–$O_b{}^{28}$ (1.912 Å), W^6–$O_c{}^{39}$ (1.902 Å) and W^6–$O_d{}^{44}$ (1.741 Å) bond lengths in PW_{11} elongate respect to P^1–$O_a{}^{14}$ (1.563 Å), W^6–$O_a{}^{14}$ (2.429 Å), W^6–$O_b{}^{29}$ (1.868 Å), W^6–$O_c{}^{40}$ (1.881 Å) and W^6–$O_d{}^{45}$ (1.70 Å) bond lengths in PW_{12}, respectively (see Scheme 1 for numbering). These results indicate a few weakening of binding interactions in PW_{11} for bonds far from lacuna position and larger changes in the bond lengths around cavity (lacuna). The bond lengths of W (4, 5, 9 and 10) atoms with O (25, 19, 32 and 38) atoms in PW_{11} respect to PW_{12} are shortened from 1.920 to 1.730 Å. This bond length shortening could be related to the high electronic density on O (25, 19, 32 and 38) atoms after removal of WO^{4+}. As mentioned, O atom's electronic density could be shifted to W and thus, strengthening of interactions.

For PW_{12}, it has been predicted that the singlet spin state ($S = 0$) is the most stable state, while the triplet ($S = 1$) and quintet ($S = 2$) spin states are 57.30 and 125.50 kcal mol^{-1} higher in energy than the singlet state, respectively (Table S1†). Also, in PW_{11} the triplet spin state is 55.86 kcal mol^{-1} higher in energy than corresponding singlet spin state.

Table 1 Selected optimized geometry parameters (bond lengths in Å) of PW_{12} and PW_{11}

	PW_{11}		PW_{12}	
Exp.[a]	Selected bond	Bond length	Selected bond	Bond length
1.530	P^1–$O_a{}^{13}$	1.563	P^1–$O_a{}^{14}$	1.597
—	P^1–$O_a{}^{14}$	1.563	P^1–$O_a{}^{15}$	1.561
2.430	W^2–$O_a{}^{13}$	2.428	W^2–$O_a{}^{14}$	2.375
—	W^6–$O_a{}^{13}$	2.429	W^6–$O_a{}^{14}$	2.516
1.900	W^2–$O_b{}^{24}$	1.867	W^2–$O_b{}^{25}$	2.061
1.900	W^6–$O_b{}^{28}$	1.868	W^6–$O_b{}^{29}$	1.912
1.910	W^2–$O_c{}^{33}$	1.881	W^2–$O_c{}^{34}$	1.893
1.910	W^6–$O_c{}^{39}$	1.881	W^6–$O_c{}^{40}$	1.902
1.690	W^2–$O_d{}^{41}$	1.700	W^2–$O_d{}^{42}$	1.745
1.690	W^6–$O_d{}^{44}$	1.700	W^6–$O_d{}^{45}$	1.741

[a] The experimental values were adapted from ref. 21 and 35.

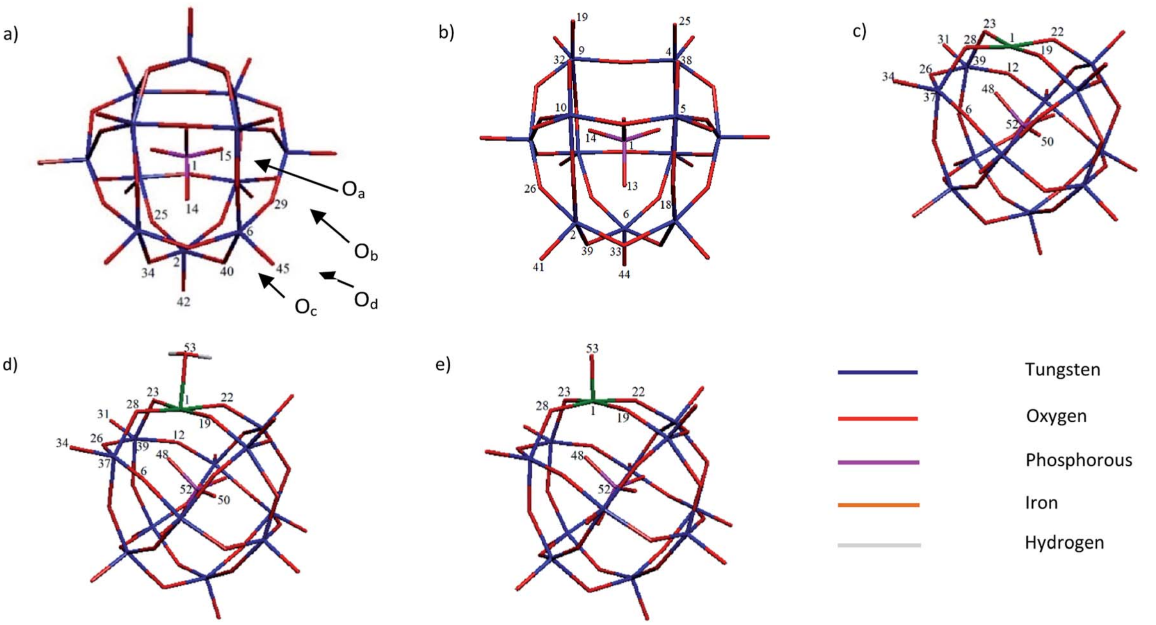

Scheme 1 The relevant numbering pattern of studied systems: (a) PW_{12}, (b) PW_{11}, (c) $PWFe^{n+}$ ($n = 2, 3$), (d) $PWFe^{n+}OH_2$ ($n = 2, 3$ and 4) and (e) $PWFe^{n+}O$ ($n = 4, 5$ and 6).

Table 2 Calculated atomic charge distributions of PW_{12} and PW_{11} determined at the NBO/UOPBE/6-31G(d) theoretical level (and LANL2DZ basis set on the metal atom)

POM	PO_4^{3-}	W	O_b	O_c	O_d
PW_{12}	−0.98	+1.98	−0.82	−0.77	−0.56
PW_{11}	−1.06	+1.67 to +1.92	−0.70 to −0.87	−0.70 to −0.82	−0.69

2.1.2. Charge distribution.

The local charge distributions on the PW_{12} and PW_{11} heteropolyanions are tabulated in Table 2.

Atomic charges of PW_{12} and PW_{11} were calculated at UOPBE/6-31G(d) level (LANL2DZ basis set on the metal atom). Although in computational context, the absolute Mulliken charges are not so accurate, their variations could be quite reliable.[21] According to the theoretical studies by Courcot and Bridgeman, the Mulliken atomic charges – compared to Hirshfeld, Voronoi Deformation Density (VDD), Quantum Theory of Atoms in Molecules (QTAIM) and the Net Total Voronoi (NTV) charges – could show the best convergence during the calculation with experimental data for several polyanions and provide a good description of Coulomb potential and their chemistry properties.[39–43] For PW_{12}, an electronic charge of $-0.98e$ is assigned for the central PO_4^{3-} moiety, which increases slightly by $-0.08e$ for PW_{11} (*i.e.* $q = -1.06e$, q is the net charge of central PO_4^{3-} in PW_{11}), and in turn constitutes the difference between local charge of central PO_4^{3-} in PW_{11} and PW_{12}. High differences between the net charges for O_d in PW_{11} ($-0.69e$) and PW_{12} ($-0.56e$) have not changed the local charge of central PO_4^{3-}. This high charge density is accumulated in the $W_{11}O_{35}$ framework of POM, especially in the terminal oxygen atoms, and increases the basicity of them.

Other prominent changes occur in atoms near the lacuna, which the positive charge of W (4, 5, 9 and 10) atoms in PW_{12} decreased from $1.98e$ to $1.67e$ in PW_{11}. This is related to the charge transfer from O (19, 25, 32 and 38) atoms in PW_{11} which bearing the high charge density after removal of WO^{4+} moiety (more information on Mulliken charges of PW_{12} and PW_{11} is presented in Table S6†).

2.1.3. Electronic structure.

The electronic structure in POMs is an important subject, owing to its direct effects on all chemical characters. The valence molecular orbitals of PW_{12} and PW_{11} were obtained by UOPBE/6-31G(d) level calculation (Fig. S1, see ESI† for MOs). As shown in Fig. S1,† for PW_{12} anion HOMO orbitals are distributed over O atoms and LUMO orbitals contain d-orbitals of W atoms with a large energy gap (2.81 eV) in the ground state. The predicted ΔE(HOMO–LUMO) of PW_{11} (amount to 2.89 eV) is similar to that of PW_{12}. Also, the nature of HOMO and LUMO in PW_{11} are similar to those of PW_{12} moiety. Thus, it could be concluded that the removal of WO^{4+} moiety from the Keggin POM does not change the HOMO and LUMO nature and also energy gap between the occupied and unoccupied orbitals.

Moreover, in order to determine the effect of additional negative charge on the valence orbital energies, six valence orbitals (α and β-spin) were selected for PW_{12} and PW_{11} compounds (Fig. 1). From Fig. 1a, among six selected α and β orbitals for PW_{12}, there are only two orbitals with negative energy and four MOs with energy close to zero. However, for PW_{11}, all mentioned orbitals possess high positive energy (Fig. 1b). The results also indicate positive energy for the interior orbitals (up to HOMO−118; no. 127). So, it can be deduced that an additional negative charge on PW_{11} increases the orbital energy. As a result, in PW_{11}, electrons are better available for

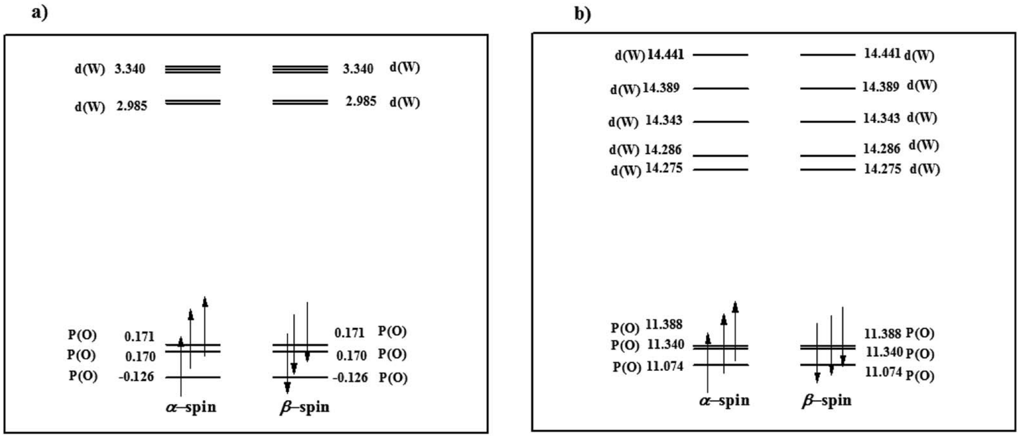

Fig. 1 Energy level expressions of frontier molecular orbitals (FMOs) for (a) PW_{12} and (b) PW_{11} in the ground state. The orbital energy values have been represented in eV.

stabilizing transition metals in different oxidation states and so PW_{11} converts to a better electron donor ligand.

Also, by removal of WO^{4+} moiety the molecular symmetry of PW_{12} reduces from T_d to C_3 in PW_{11}. Decent in symmetry leads to lifting the doublet-triplet degeneracy in d_{xy}-like orbitals[21] of PW_{12} and singlet degeneracy for all orbitals performs in PW_{11} (Fig. 1).

2.1.4. Simulated infrared spectra (IR). From the optimized geometries of PW_{12} and PW_{11}, it is revealed that by removing one WO^{4+} moiety from PW_{12} the P–O_a, W=O_d, W–O_b–W and W–O_c–W bond lengths in PW_{11}, which are far from lacuna site, would increase. IR spectroscopy being able to detect small structural differences and so, is a sufficient probe for investigation of the variation of Keggin-type POM structures. Keggin-type POMs, as metal–oxygen clusters, contain some of metal–oxygen stretching vibrational modes at 500–1100 cm^{-1}. Accordingly, based on vibrational frequency calculations, simulation of IR spectrum of PW_{12} and PW_{11} have been done at OPTX-PBE/DZVP-GGA level.

For PW_{12} structure, four infrared absorption bands at 1067, 963, 863 and 790 cm^{-1} have been assigned to P–O_a, W=O_d, W–O_b–W and W–O_c–W stretching bonds, respectively. From literature, it has been established that DFT methods generate IR vibrational frequencies with a slight shift towards low energies.[44] As to PW_{11}, the P–O_a stretching mode exhibits a splitting to two components at 1060 and 1050 cm^{-1} which is approved by experimental data.[45] Moreover, the vibrational frequencies of P–O_a, W=O_d, W–O_b–W and W–O_c–W bonds in PW_{11} at 1060, 1050, 871, 800 and 706 cm^{-1}, in comparison with PW_{12}, are appeared at lower frequencies. The results of IR spectrum calculations, that verify the modification in PW_{11} geometry, are tabulated in Table 3 (and also Fig. S3 and S4†).

2.2. Ground state geometries, charge distribution, electronic structure, and simulated infrared spectra of $PWFe^{n+}$ and $PWFe^{n+}OH_2$ (n = 2 and 3)

In respect to the role of TMSPOMs in different reactions like oxidative and acid/base processes[46–50] and also the effective role of iron substituted POMs,[51] various Fe oxidation states in iron substituted Keggin type POMs have been studied in this work. As stated above, truncation of PW_{12} by removing of WO^{4+} moiety leaves behind a lacunary PW_{11} which act as a ligand and in combination with Fe generates $PWFe^{n+}$ (n = 2 and 3) as iron substituted POMs. By locating a H_2O ligand at the sixth octahedral coordination position, the $PWFe^{n+}OH_2$ (n = 2 and 3) cluster would be formed.

2.2.1. Ground state geometries. It is well known that the spin state of each complex is depended on its environment and especially the nature of their ligands.[52,53] In the $PWFe^{n+}$, the ground state geometry of $Fe^{II/III}$ substituted POM structures have been optimized at the spin-unrestricted OPTX-PBE/DZVP-GGA level. For POM–Fe^{II}, three spin states of singlet ($S = 0$), triplet ($S = 1$) and quintet ($S = 2$) have been considered. It was predicted that the quintet spin state ($S = 2$) is the most stable state, while the singlet ($S = 0$) and triplet ($S = 1$) spin states are 23.53 and 12.43 kcal mol^{-1} less stable, respectively. Moreover, for Fe^{III} substituted POM, among three considered spin states (S = 1/2, 3/2, 5/2), it has been predicted that the sextet ($S = 5/2$) is the most stable while doublet ($S = 1/2$) and quartet ($S = 3/2$) spin states are roughly 23.03 and 8.16 kcal mol^{-1} less stable, respectively.

Also, the structure of $PWFe^{II}OH_2$ was optimized in three spin states singlet ($S = 0$), triplet ($S = 1$) and quintet ($S = 2$). From the results, it has been unravelled that quintet state ($S = 2$) is the

Table 3 Calculated vibrational frequencies (cm^{-1}) and assigned bands of PW_{12} and PW_{11} determined at OPTX-PBE/DZVP-GGA level

	Vibrational frequency/cm^{-1}	
Stretching mode	PW_{11}	PW_{12}
$\nu_{(P-O_a)^1}$	1060	1067
$\nu_{(P-O_a)^2}$	1050	—
$\nu_{(W=O_d)}$	871	963
$\nu_{(W-O_b-W)}$	800	863
$\nu_{(W-O_c-W)}$	706	790

most stable while singlet ($S = 0$) and triplet ($S = 1$) spin states are 23.53 and 12.49 kcal mol^{-1} less stable, respectively. Our attempts failed in determination a local minimum for interacting of H_2O and Fe^{II} in triplet and quintet spin states since the weak iron–water interaction results in separation of H_2O following optimization and then their interaction with O^{28} of POM through hydrogen bond has been exhibited. Consequently, the singlet spin state is more favourable for this Fe substituted POM in an oxidation process, because Fe interacts directly with H_2O ligand. At higher spin states, electron transfer from Fe^{II} d orbitals of antibonding MOs of Fe–OH_2 bond leads to weakening the interaction between H_2O and Fe, and so dissociation of H_2O following optimization of corresponding geometry. The same holds true for $PWFe^{III}OH_2$ at doublet, quartet and sextet spin states, where doublet spin state is more appropriate because Fe interacts directly with H_2O. As shown in Fig. 2, $PWFe^{n+}OH_2$ ($n = 2$ and 3) which is generated through replacing WO^{4+} moiety with [Fe–OH_2] in PW_{12} is optimized at doublet, quartet and sextet spin states for Fe^{III} and singlet, triplet and quintet spin states for Fe^{II} (see ESI† for *xyz* coordinates of studied systems).

Key geometry parameters of $PWFe^{n+}$ and $PWFe^{n+}OH_2$ ($n = 2$ and 3) are tabulated in Table S2.† In $PWFe^{II}$, as the total charge reduced from -7 to -5 respect to PW_{11}, the bond lengths are also shortened, while these are still long respect to PW_{12}. This implies that by changing the electron density on atoms the whole system remained stable but some of the bond lengths are altered. The most important alterations in the bond lengths have been predicted in the bonds around lacuna region in POM. The W–O bond length nearby the lacuna, which their oxygen atoms are ligated to Fe^{II}, increases from 1.730 Å in PW_{11} to 1.808 Å in $PWFe^{II}$ (Table S2†). Substitution of Fe in PW_{11} is along with significant charge distribution from oxygen atoms to Fe. The charges of Fe, W (35, 37, 39 and 44) and O donor atoms (19, 22, 23 and 28) in $PWFe^{II}$ are 0.67*e*, 1.86*e* and $-0.69e$ respectively, which in compare with charges of W (4, 5, 9 and 10) and O donor atoms (19, 25, 32 and 38) in PW_{11} (1.70*e* and $-0.63e$ respectively), the positive charge of W atoms is increased. Thus the bond length for W^{37}–O_c^{28} (1.808 Å) is predicted to be shorter and stronger with respect to Fe^1–O_c^{28} (1.932 Å). The difference predicted between Fe^1–O_a^{48} (1.938 Å) and W^{37}–O_a^{48} (2.460 Å) bond lengths shows the stronger interaction between Fe and O_a^{48} (centre tetrahedral oxygen) respect to W^{37}–O_a^{48}, even though Fe^{II} and W^{VI} radiuses are almost equal. This is because the bond length depends on both of the M–O interaction and metal radius. Also, the stronger interaction can be related to the favourable orientation of Fe d_{z^2} orbital with O_a^{48} pz orbital and not to the charge distribution, because the charge of O_a^{48} (-0.76) in $PWFe^{II}$ compared with O_a^{13} (-0.74) in PW_{11} was not changed significantly. In $PWFe^{III}$, single electron oxidation of Fe^{II} into Fe^{III} caused the shortening of all above mentioned bond lengths. This implies that bonding interaction between Fe^{III} atom and four oxygen atoms of POM lacuna is stronger than that of Fe^{II}.

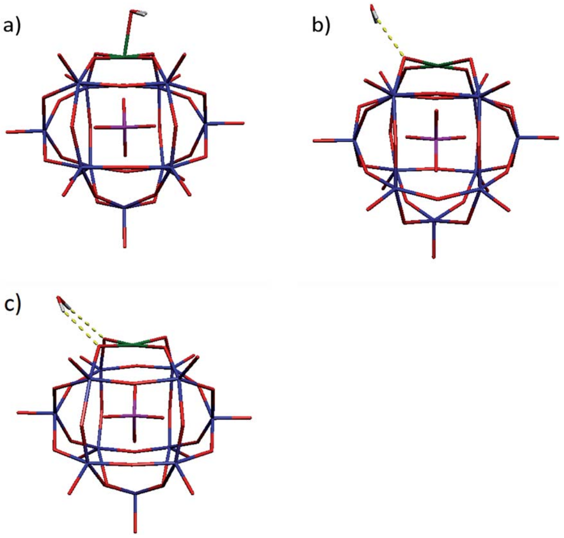

Fig. 2 The optimized geometry of $PWFe^{II}OH_2$ (a) in the singlet, (b) in the triplet and (c) in the quintet spin states obtained by OPTX-PBE/DZVP-GGA calculation.

Our calculation also shows small structural differences between $PWFe^{n+}$ and $PWFe^{n+}OH_2$ ($n = 2$ and 3) (Table S2†). A slight structural change has been exhibited when H_2O ligated on Fe and so Fe^1–O_a^{48} (see Scheme 1 for labelling) bond length become longer in $PWFe^{n+}OH_2$ ($n = 2$ and 3) (*i.e.* $q = 0.044$ Å) and is the difference in Fe^1–O_a^{48} bond length between $PWFe^{II}$ and $PWFe^{II}OH_2$. The large Fe^1–O_a^{48} length shows a weak bonding interaction which provides an unsaturated metal atom in pseudo-octahedral coordinated sphere.[19,30,31] Thus, Fe has an additional ability for binding to H_2O ligand. It is well-known that POMs have excellent structural stability while accepting or donating one or several electrons in various chemical mediums. Along with our study, the geometric parameters of POMs were checked for single electron oxidation of iron in POM (Fe^{II} to Fe^{III}). As expected, no significant structural changes were predicted and only the geometric parameters of Fe–OH_2 bond have been influenced. The Fe^{II}–O_{aqua} and Fe^{III}–O_{aqua} bond lengths were 2.113 Å and 2.060 Å respectively, and $\Delta r(Fe^{III/II}$–$O_{aqua}) = 0.053$ Å.

The bonding nature has also been investigated using NBO analysis. The calculated WBI (Wiberg Bond Index) values for Fe^{II}–OH_2 and Fe^{III}–OH_2 are 0.3358 and 0.3759, respectively (Table S2†). Thus, there is a single and weak bonding interaction between Fe^{II} and Fe^{III} with H_2O molecule.

2.2.2. Charge distribution.

The computed atomic charge distributions for $PWFe^{n+}$ and $PWFe^{n+}OH_2$ ($n = 2$ and 3) are tabulated in Table 4 and can be described as follows:

(i) The $O_b(W_2)$ and $O_c(W_2)$ charges in Fe-substituted systems are similar to that of PW_{12} and PW_{11}. The higher negative charges of bridged oxygen atoms, $O_b(W_2)$ and $O_c(W_2)$ with values between $-0.82e$ and $-0.77e$, than terminal oxygen atoms have revealed higher basicity of bridged oxygen atoms.

(ii) In these systems, because of shorter bond lengths, favourable orientations and so higher negative overlap in terminal metal–oxygen bonds are expected. Also, transfer charges from O_d ($-0.63e$) to tungsten are predicted to be more than those of O_b ($-0.82e$) and O_c ($-0.78e$) as bridged oxygen

Table 4 Calculated atomic charges of $PWFe^{n+}$ and $PWFe^{n+}OH_2$ ($n = 2$ and 3) determined based on the NBO/UOPBE/6-31G(d) level (LANL2DZ basis set on the metal atom)

Atom/group	$PWFe^{II}$	$PWFe^{II}OH_2$	$PWFe^{III}$	$PWFe^{III}OH_2$
PO_4	−0.96	−0.96	−0.97	−0.94
O_d	−0.63	−0.63	−0.60	−0.60
O_{48}	−0.78	−0.76	−0.76	−0.74
O_b (W_2)	−0.82	−0.82	−0.83	−0.82
O_b (FeW)	−0.70	−0.70	−0.72	−0.72
O_c (W_2)	−0.78	−0.78	−0.78	−0.77
O_c (FeW)	−0.67	−0.69	−0.68	−0.70
Fe	0.67	0.64	0.85	0.66
W	1.90	1.91	1.95	1.95
O_{aqua}	—	−0.90	—	−0.75

atoms. These results state that $W{=}O_d$ bond (1.720 Å) is stronger and shorter than $W–O_b$ (1.945 Å) and $W–O_c$ (1.967 Å) bonds.

(iii) The negative charges on bridge and corner oxygen atoms in O_b (W_2) and O_c (W_2) are larger than those of bridge and corner oxygen atoms in O_b (FeW) and O_c (FeW). This indicates more charge transfer effect from these oxygen atoms to Fe.

(iv) For PW_{12}, the Mulliken analysis assigns an electronic charge of $-0.98e$ on PO_4^{3-}. Slightly decreasing in the negative charge on PO_4^{3-} in Fe-substituted POM indicates that Fe substitution in POM does not change the net charge on PO_4^{3-}. So, additional charges from substitution of Fe^{n+} ($n = 2$ and 3) instead of WO^{4+} moiety in Keggin POM may be directed to $W_{11}O_{35}$ framework of POM and specially concentrated in terminal oxygen atoms. As it could be seen, the charges on terminal oxygen atoms in these systems are greater than those of PW_{12}. Accumulation of charge density in the terminal oxygen atoms of Keggin POMs shows a relationship between the basicity of terminal oxygen atoms and the number and type of substituted metals. Also, in electron transfer reactions of Keggin POMs, additional electron transfers to the terminal oxygen atoms and the POM structure occur without significantly deforming in the framework. For this reason, the Keggin POMs are of interest in oxidation catalysis.[21,54–56]

(v) Different atoms in $PWFe^{n+}$ resemble the charges on $PWFe^{n+}OH_2$ ($n = 2$ and 3), except the positive charge on Fe which decreases after H_2O placing. The charge reduction for oxidation state III is more than oxidation state II. This implies a charge reorganization or transfer from O atom of H_2O ligand to Fe and reduction of positive charge on Fe atom.

2.2.3. Fe–POM interactions based on electronic structure. The energy level scheme of the MOs obtained from optimized $PWFe^{n+}$ and $PWFe^{n+}OH_2$ ($n = 2$ and 3) structures is shown in Fig. 3. As shown, following substitution of Fe^{II} in PW_{11} lacuna, the d orbitals of Fe^{II} are distributed between d(W) and p(O) orbitals of PW_{11} (Fig. 3a). In this diagram five MOs (HOMO−2, HOMO−1, HOMO, LUMO and LUMO+1) are metal-based d orbitals and responsible for bonding interaction between Fe atom and four oxygen atoms of PW_{11}. More accurate analysis of the MOs shows that 2p orbitals of oxygen atoms (19, 22, 23 and 28) and d orbitals of Fe have the most important contribution in obtaining those valance MOs, having significant metal character (>70%). Moreover, based on the NBO analysis, the electronic structure of $PWFe^{II}$ has been studied. The calculated NBO partial charges of these complexes are listed in Table 4. From the results the charge of Fe is $0.67e$.

Compared with the free metal ion, lower magnitude of positive charge on Fe indicates charge reorganization or transfer from Keggin-type POM cage to the transition metal center, which is in well agreement with the MO prediction. Increasing of the Fe oxidation state from II to III is along with an increasing in oxygen 2p-orbital contribution (19, 22, 23 and 28) in PW_{11} indicating a stronger interaction between Fe^{III} and PW_{11}. This is mainly due to lower energy gaps between Fe^{III} d orbitals and oxygen 2p orbitals in PW_{11} than that of Fe^{II} ion. By linking H_2O ligand to iron, the orbital energies and configuration of electronic structure in $PWFe^{II}OH_2$ do not change, in respect to $PWFe^{II}$ (Fig. 3b). Bonding interaction between Fe and H_2O ligand is accompanied by overlapping between $\sigma(b_2)$ non-bonding orbital of H_2O ligand and $3d_{z^2}$ orbital of Fe leading to a weak σ bonding interaction. A charge transfer from H_2O oxygen atom to Fe could be occurred after this σ interaction,[57,58] and so, in $PWFe^{III}$ the interaction of metal center with H_2O becomes stronger. Moreover, orbital energies for $PWFe^{n+}$ and $PWFe^{n+}OH_2$ ($n = 2$ and 3) decrease by changing the Fe^{II} to Fe^{III} in a significant manner (Fig. 3).

2.2.4. Simulated infrared spectra. The IR spectra of selected systems ($PWFe^{n+}$ and $PWFe^{n+}OH_2$; $n = 2$ and 3) have also been determined. From the results in Table 5 (and Fig. S5–S8†), $P–O_a$ asymmetric stretching vibration at 1067 cm^{-1} in α-PW_{12} splits into two IR bands in PW_{11}. Iron substitution at lacuna position of PW_{11} – which contains donor oxygen atoms – and formation of $PWFe^{n+}$ ($n = 2$ and 3) again results in one IR single band for $P–O_a$. This is also observed for the most of mono transition metal substituted Keggin type POMs.[20,59] Moreover, the $W–O_c–W$ band in PW_{12} is splitted into $W–O_c–W$ and $W–O_c–Fe$ IR bands in $PWFe^{n+}$ ($n = 2$ and 3).[20] Meanwhile, in these two POMs $W{=}O_d$ and $W–O_b–W$ vibrations, compared to α-PW_{12}, shifted to lower energies. Therefore, five characteristic bands could easily be employed to identify the structure of $PWFe^{n+}$ ($n = 2$ and 3) POMs.[59] For simulated vibrational spectrum of $PWFe^{n+}OH_2$ compared with that of $PWFe^{n+}$ ($n = 2$ and 3), the IR band of $P–O_a$ is predicted to shift by 12 cm^{-1} upon linking to H_2O (Table 5, and Fig. S5–S8†). However, $W{=}O_d$, $W–O_b–W$, $W–O_c–Fe$ and $W–O_c–W$ vibrations are not significantly shifted which indicate that these vibrational bands are not sensitive to H_2O ligation.

According to the simulated IR spectrum of $PWFe^{n+}OH_2$ ($n = 2$ and 3), the symmetric stretching and bending vibrational frequencies of H_2O are similar in both complexes. This is mainly due to weak interaction between H_2O and iron atoms in both of Fe oxidation states. By increasing the Fe oxidation state (from +2 to +3), all vibrational frequencies of $P–O_a$, $W{=}O_d$, $W–O_b–W$ and $W–O_c–W$ bonds in simulated IR spectrum move towards higher frequencies which is compatible with corresponded bond lengths.

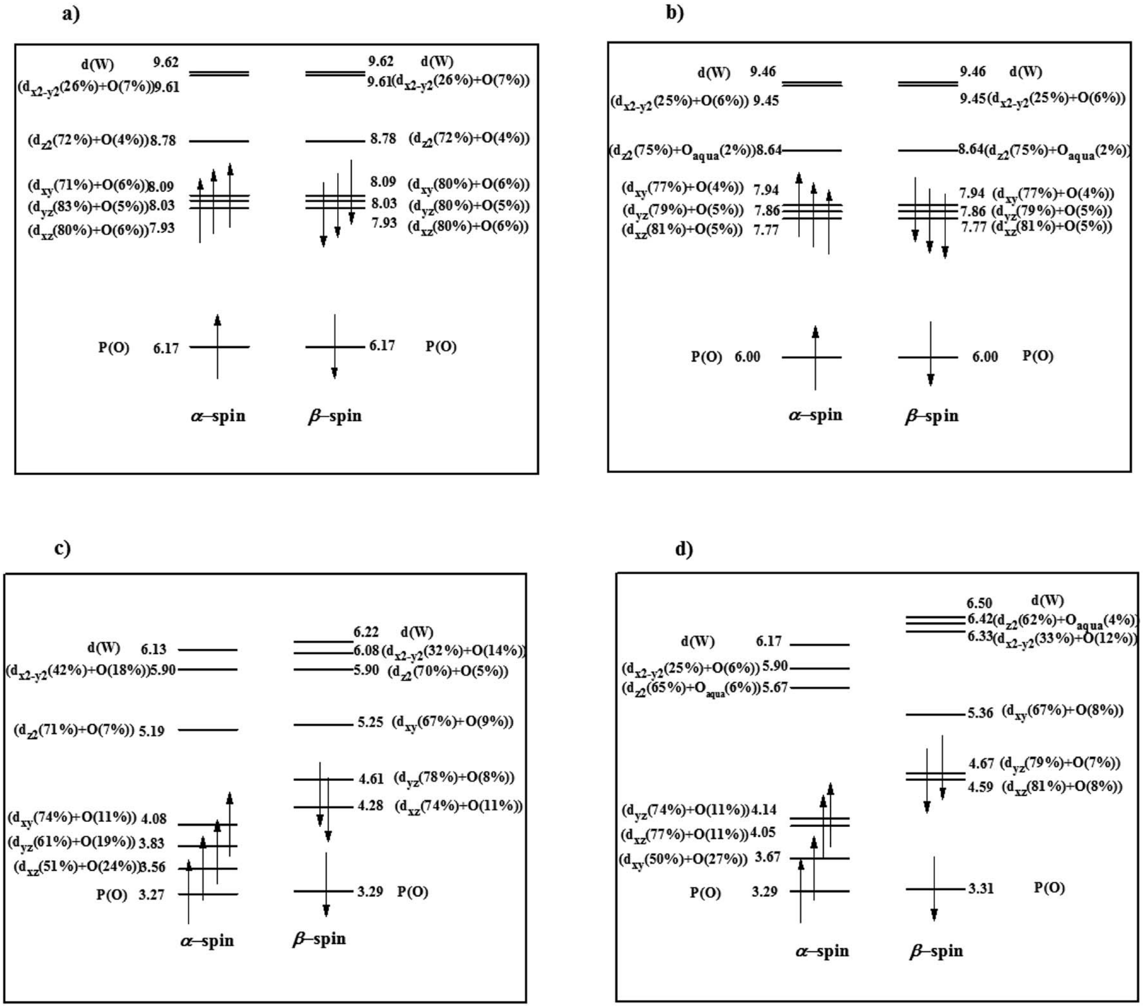

Fig. 3 The energy level expressions of frontier MOs for (a) PWFe^{II}, (b) PWFe^{II}OH$_2$, (c) PWFe^{III} and (d) PWFe^{III}OH$_2$ at ground state calculated at UOPBE/6-31G(d) level (LANL2DZ basis set on the metal atom). The orbital energy values have been represented in eV.

2.3. High-valent PWFe^{IV}(OH$_2$/OH) and PWFe$^{IV/V/VI}$(O) substituted POMs

TMSPOMs are of major importance in oxygenation of organic compounds.[3,4,60–66] In the oxidative process, high-valent TMSPOMs are usually generated by interaction of low-valent substituted transition metals with oxidant or other species available in the reaction medium and exhibited improved catalytic behaviours. Study on these high-valent TMSPOMs is essential for determining and characterizing their active species in reaction mediums. To our knowledge, rare studies on geometry, electronic structure and activity of high-valent TMSPOMs have been reported in literature. The quantum chemistry calculations based on DFT are applicable tools to shed more light on this context. A detailed DFT study on geometry, electronic structure and chemical bonding features of important high-valent species consist of $[PW_{11}O_{39}(Fe^{IV}OH_2)]^{3-}$ (PWFe^{IV}OH$_2$), $[PW_{11}O_{39}(Fe^{IV}OH)]^{4-}$ (PWFe^{IV}OH), $[PW_{11}O_{39}(Fe^{IV}O)]^{5-}$ (PWFe^{IV}O), $[PW_{11}O_{39}(Fe^{V}O)]^{4-}$ (PWFe^{V}O), and $[PW_{11}O_{39}(Fe^{VI}O)]^{3-}$ (PWFe^{VI}O) were done at the OPTX-PBE/DZVP-GGA level. High-valent $[PW_{11}O_{39}(Fe^{n+}O)]^{(9-n)-}$ (PWFe^{n+}O; $n = 4, 5, 6$) species constitute important intermediates in

Table 5 Selected vibrational frequencies (cm^{-1}) of POM complexes determined at OPTX-PBE/DZVP-GGA level

POM	2S + 1	$\nu_{(P-O_a)}$	$\nu_{(W=O_d)}$	$\nu_{(W-O_b-W)}$	$\nu_{(W-O_c-W)}$	$\nu_{(W-O_c-Fe)}$	$\nu_{(H-O-H)}$	$\nu_{(H-O-H)}$	$\nu_{(H-O-H)}$
PWFe^{III}	2	1092	942	843	778	756	—	—	—
PWFe^{III}OH$_2$	2	1080	941	844	777	756	1684	3636	3732
PWFe^{II}	1	1072	921	831	769	738	—	—	—
PWFe^{II}OH$_2$	1	1061	921	834	775	731	1689	3635	3716

oxidation processes. These oxidized species could have terminal Fe═O bond as an essential active site in catalytic oxygenation reactions. For terminal W═O bonds, because of π*-antibonding unoccupied orbitals, their bonding interactions lie in very high energy and so are not available for interaction with substrates.[32] In this section, at first the geometry, electronic structure and chemical bonding features of seven considered species will be deliberated, and then favourable species for oxidation reactions will be addressed.

2.3.1. $PWFe^{IV}OH_2$ and $PWFe^{IV}O$ species. The $PWFe^{IV}OH_2$, as one of the high-valent species generated in the oxidation process, has three possible spin states of singlet, triplet, and quintet. From the results, singlet spin state is higher in energy than triplet by 7.4 kcal mol^{-1}. As for quintet spin state, weak interaction between Fe^{IV} and H_2O leads to the separation of H_2O from Fe and interaction with 23 and 29 oxygen atoms of lacuna POM through H_2O hydrogen atoms. For triplet spin state of $PWFe^{IV}OH_2$, the optimized geometry revealed a 2.047 Å bond length for Fe^{IV}–OH_2. The calculated WBI value for Fe^{IV}–O_{aqua} bond in $PWFe^{IV}OH_2$ is 0.384 (Table S3†). Thus, Fe^{IV}–OH_2 is a weak single bond and consequently terminal Fe═O bond could not exist in $PWFe^{IV}OH_2$. As previously mentioned, POMs can accept or donate one or several electrons with minimal structural changes,[27,30] thus our focus was not concentrated on bond lengths in this POMs (Table S3†). To verify, similarity in the IR frequencies of high-valent TMSPOMs have been shown by calculation (Table S4 and Fig. S9–S13†).

Bond length and bonding interaction in Fe^{IV}–OH_2 has not much difference with those of low-oxidation state species $PWFe^{III}OH_2$. Thus, Fe–O_{ligand} bond length is decreased from 2.060 Å in $PWFe^{III}OH_2$ to 2.047 Å in $PWFe^{IV}OH_2$ (Δr(Fe–OH_2) = 0.013 Å) and so the electronic structures of $PWFe^{III}OH_2$ and $PWFe^{IV}OH_2$ are almost similar. From the orbital energies of $PWFe^{IV}OH_2$ calculated through UOPBE/6-31G(d) level (LANL2DZ basis set on the metal atom), five MOs of HOMO−2, HOMO−1, HOMO, LUMO and LUMO+1 (Fig. S2a†) are metal-based d orbitals with antibonding character. These are originated from the overlapping between d orbitals of Fe and oxygen p orbitals (19, 22, 23 and 28). From the interaction between Fe $3d_{z^2}$ orbital and σ(b2) non-bonding orbital of H_2O, a σ* molecular orbital could be formed.

Also, the inspection of molecular orbital diagram in this compound indicates that the π*-antibonding orbital, which is responsible for Fe═O bond, is not formed (Fig. S2a†). This expression of electronic configuration which made by molecular orbital analysis could be confirmed by Mulliken spin population. Obviously, the spin densities contribute in determining the electronic structure in all POM compounds. The spin density of $PWFe^{IV}OH_2$ in its triplet ground state is mainly localized on Fe^{IV} (1.6) and partly on the four coordinated oxygen atoms of PW_{11} (0.085). No spin density resides on O_{aqua} (−0.015) being in well agreement with the MO prediction (Table 6).

Geometry structure of the other high oxidation state Fe substituted POMs, $PWFe^{IV}OH$, was also optimized at OPTX-PBE/DZVP-GGA level. As results show, triplet state ($S = 1$) is the most stable and for singlet ($S = 0$) and quintet ($S = 2$) spin states lower stabilities up to 11.1 and 4.8 kcal mol^{-1} were obtained, respectively. From the key geometrical parameters tabulated in Table S3,† by OH ligand in place of H_2O, interaction between Fe^{IV} and OH in a significant manner is improved. Thus, the optimized Fe^{IV}–O_{ligand} bond length is decreased from 2.047 Å in $PWFe^{IV}OH_2$ to 1.815 Å in $PWFe^{IV}OH$ (Δr(Fe–O_{ligand}) = 0.232 Å). The calculated WBI value for Fe^{IV}–OH is 0.9089 and so Fe^{IV}–OH bond is a strong single bond.

Table 6 Calculated atomic charges and spin density of OH_2, OH, O and Fe atoms in $PWFe^{II-VI}$ species determined based on NBO/UOPBE/6-31G(d) level (LANL2DZ basis set on the metal atom)

POM	Charge of O_{ligand}	Charge of Fe	Spin density of O_{ligand}	Spin density of Fe
$PWFe^{II}OH_2$	−0.90	0.64	0	0
$PWFe^{III}OH_2$	−0.75	0.66	−0.008	0.924
$PWFe^{IV}OH_2$	−0.73	0.82	−0.01	1.595
$PWFe^{IV}OH$	−0.64	0.87	0.10	1.713
$PWFe^{IV}O$	−0.43	0.86	0.76	3.072
$PWFe^{V}O$	−0.37	0.96	0.81	1.986
$PWFe^{VI}O$	−0.31	1.11	0.46	1.332

According to our calculations, significant change on the Fe–OH bond in $PWFe^{IV}OH$ demonstrates different electronic structure from $Fe^{II/III/IV}$–OH_2 POMs (Fig. S2b†). Among five frontier molecular orbitals that are metal-based d orbitals, two are responsible for Fe–OH bonding interaction. The σ(p–d) orbital come from overlapping between $2p_z$ orbital of OH ligand with $3d_{z^2}$ orbital of Fe.

Also, the π*-antibonding orbitals arise from the interaction among $3d_{xz}$ orbital of Fe and $2p_x$ from oxygen in OH. It is well known that Fe–O_{ligand} π*-antibonding unoccupied orbital is closely correlated to the catalytic oxygenation processes, because it provides an electronic clue for reactivity in oxygen transfer reactions. Therefore, $PWFe^{IV}OH$ with unoccupied π^*_{xz}-antibonding orbital may have a better reactivity for oxygen transfer reaction.[67,68]

2.3.2. The effect of Fe oxidation state in defining favourable catalyst for oxygen transfer. In the next step, high-oxidation state iron substituted POMs with oxo ligand, $PWFe^{n+}O$ ($n = 4$, 5 and 6), in various spin states optimized at DFT/OPTX-PBE/DZVP-GGA level have been investigated. According to the results, $PWFe^{IV}O$, $PWFe^{V}O$ and $PWFe^{VI}O$ have triplet, quartet, and triplet ground spin states respectively.

In $PWFe^{IV}O$, decreasing in Fe^{IV}–O_{ligand} bond length to 1.641 Å in the triplet ground state, compared to 1.815 Å for $PWFe^{IV}OH$, could be confirmed by calculation of WBI value for Fe^{IV}–O_{ligand} which is 1.46. Moreover, this shows a significant double bond feature for Fe^{IV}–O_{ligand} (Table S3†). Analysis of Fe^{IV}–O bonding interaction by electronic structure shows that HOMO and HOMO−1 orbitals are responsible for metal–oxygen binding interaction (Fig. S2c†). Both orbitals are obtained from significant contribution of oxygen $2p_{x/y}$ orbitals and $3d_{xz/yz}$ orbitals of Fe^{IV}. It should be noted that, these orbitals have important Fe–O_{ligand} π*-antibonding character. Among that, $3d_{xy}$ orbital is destabilized by antibonding interactions with p orbitals of four donor oxygen atoms at lacuna POM. As mentioned above, this important unoccupied Fe–O_{ligand} π*-antibonding orbitals do not exist in $Fe^{II/III/IV}$–OH_2 POMs.

In $PWFe^{V}O$, optimized structure of the low energy triplet spin state show that Fe^{V}–O_{ligand} bond length decreases to 1.635 Å from 1.641 Å in Fe^{IV}–O. This demonstrates minor changes in Fe^{V}–O_{ligand} compared to Fe^{IV}–O_{ligand} bond. This is mainly due to electron removing from nonbonding $3d_{xy}$ orbital (β-HOMO) in Fe^{V}–O respect to Fe^{V}–O_{ligand} bond. From the previous experimental studies by Rong and co-workers, $[PW_{11}O_{39}(Ru^{V}O)]^{4-}$ possesses high capability in oxygen-transfer reaction.[69,70] It is worth mentioning that in the most of oxygen transfer reactions, at first, one electron transfers from $\pi_{c=c}$ orbital of alkene to π^*_{oxo} orbital of M=O. This would weaken the M=O bond and then oxygen transfer from M=O group to alkene will happen.[71,72] Hence, $PWFe^{V}O$ could be a favourable species in these reactions due to some of advantages that will be discussed in the following.

For optimized $PWFe^{VI}O$, the Fe^{VI}–O_{ligand} bond length decreases to 1.601 Å in the triplet ground state from 1.635 Å in $PWFe^{V}O$ ($\Delta r(Fe^{V/VI}$–$O_{ligand}) = 0.034$ Å). Also, calculated WBI value for Fe^{VI}–O_{ligand} was 1.542 which indicates a significant double bond feature (Table S3†). In view of that, $PWFe^{VI}O$ bonding interaction and subsequently their electronic structure are similar to $PWFe^{IV/V}O$.

As mentioned above, the important unoccupied Fe=O π*-antibonding orbitals are absent in $PWFe^{II/III/IV}OH_2$ while they appear in $PWFe^{IV/V/VI}O$. Mulliken spin population analysis also supports these interactions and electronic structures. Spin density in these compounds is mostly localized on Fe=O moiety and some of that on four oxygen in lacuna position of PW_{11}, while the rest of POM cage carry a small negative spin density (Table 6).

Now the question is: which of these high-oxidation states Fe substituted POMs would be favourable for oxidation process. According to frontier molecular orbital (FMO) theory, a suitable oxidation catalyst requires unoccupied orbitals with low energy and high orbital contribution of reactive atom at LUMO to achieve an appropriate overlap with the reagent FMOs.[67,68,73,74] The energy expression and participation percentage of Fe and oxygen in unoccupied Fe=O π*-antibonding orbitals are shown in Fig. 4.

As it could be seen in Fig. 4, in $PWFe^{IV/V}O$ species, unoccupied Fe=O π*-antibonding orbitals consist of β spin orbitals. In $PWFe^{VI}O$, unoccupied Fe=O π*-antibonding orbitals consist of α and β spin orbitals. Respect to HOMO, which contains oxygen p-orbitals, the energies of unoccupied Fe=O π*-antibonding orbitals decrease in the following order: $PWFe^{IV}O > PWFe^{V}O > PWFe^{VI}O$ (Fig. 4). This order could be attributed to the POM charges reducing.[75–77] Contribution of oxygen atom orbitals in these unoccupied Fe=O π*-antibonding orbitals decreases as following: $PWFe^{V}O > PWFe^{IV}O > PWFe^{VI}O$ (Fig. 4).

Calculated atomic charges and spin density values of oxygen bonded Fe in $PWFe^{IV/V/VI}O$ species are tabulated in Table 6. Results in Table 6 show lower negative charge for O^{2-} ligand in these TMSPOMs than free O^{2-}. Lesser negative charge on O^{2-} ligand indicates the charge transfer from oxygen to Fe. Therefore, polarization of Fe=O bond could be an important factor for determining the activity differences in these TMSPOMs. The absolute values of atomic charges decrease in the following order: $PWFe^{IV}O$ (−0.43) > $PWFe^{V}O$ (−0.37) > $PWFe^{VI}O$ (−0.31) (Table 6). This is mainly along with increasing in the oxidation state of Fe atom. Moreover, decreasing in the spin density of O^{2-} ligand for these high-oxidation state species is as following: $PWFe^{V}O > PWFe^{IV}O > PWFe^{VI}O$ (Table 6). In both of $PWFe^{IV/V}O$ species, with high spin density on the O^{2-} (0.76 and 0.81 respectively), the O^{2-} ligand possess substantial radical character. In experimental reports, radical complexes are regarded as suitable catalysts for closure of the epoxide rings.[20] In contrary, radical character of oxygen in $PWFe^{VI}O$ is weakened considerably where the calculated spin density on the O^{2-} decreased to 0.46.

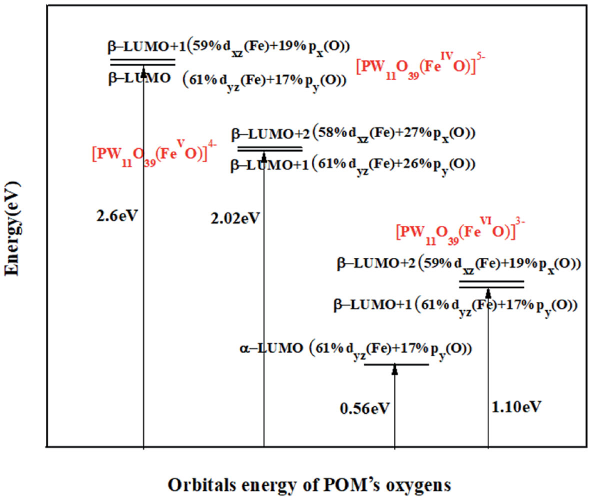

Fig. 4 Unoccupied Fe=O π*-antibonding orbitals for high-oxidation states $PWFe^{IV/V/VI}O$ determined based on UOPBE/6-31G(d) level (LANL2DZ basis set on the metal atom).

According to above mentioned points, $PWFe^{V}O$ would be favorable for oxidation processes owing to unoccupied π*-antibonding orbitals (β-LUMO+1 and β-LUMO+2) with low energy and high contribution of O^{2-} respect to $PWFe^{II/III/IV}OH_2$, $PWFe^{IV}OH$ and $PWFe^{IV/VI}O$. From the FMOs energy expression of $PWFe^{V}O$ in Fig. 5, it could be revealed that: α and β occupied and unoccupied orbitals with π* symmetry (α-HOMO−2, α-HOMO−3, β-LUMO+1, β-LUMO+2) and α and β unoccupied orbitals with σ* symmetry (α-LUMO+1 and β-LUMO+8) are responsible for Fe=O bonding interaction in $PWFe^{V}O$. The π*-antibonding orbitals are formed from overlapping between $3d_{xz/yz}$ orbitals of Fe^{V} and $2p_{x/y}$ orbitals of oxygen, while the σ*-antibonding orbitals are made from combining the $3d_{z^2}$ orbital of Fe^{V} and $2p_z$ orbital of O^{2-} ligand. Due to their lower energy, unoccupied π* orbitals are more important than σ* ones. According to DFT results, unoccupied Fe=O π*-antibonding orbitals comprise from β-LUMO+1 and β-LUMO+2 in which β-LUMO+1 (π^*_{yz}) contain 26% contribution of O^{2-} p_y orbital and 61% Fe^{V} d_{yz} orbital and β-LUMO+2 (π^*_{xz}) contains 27% contribution of O^{2-} p_x orbital and 58% of Fe^{V} d_{xz} orbital which are mostly classified as Fe=O functional group (Fig. 4).

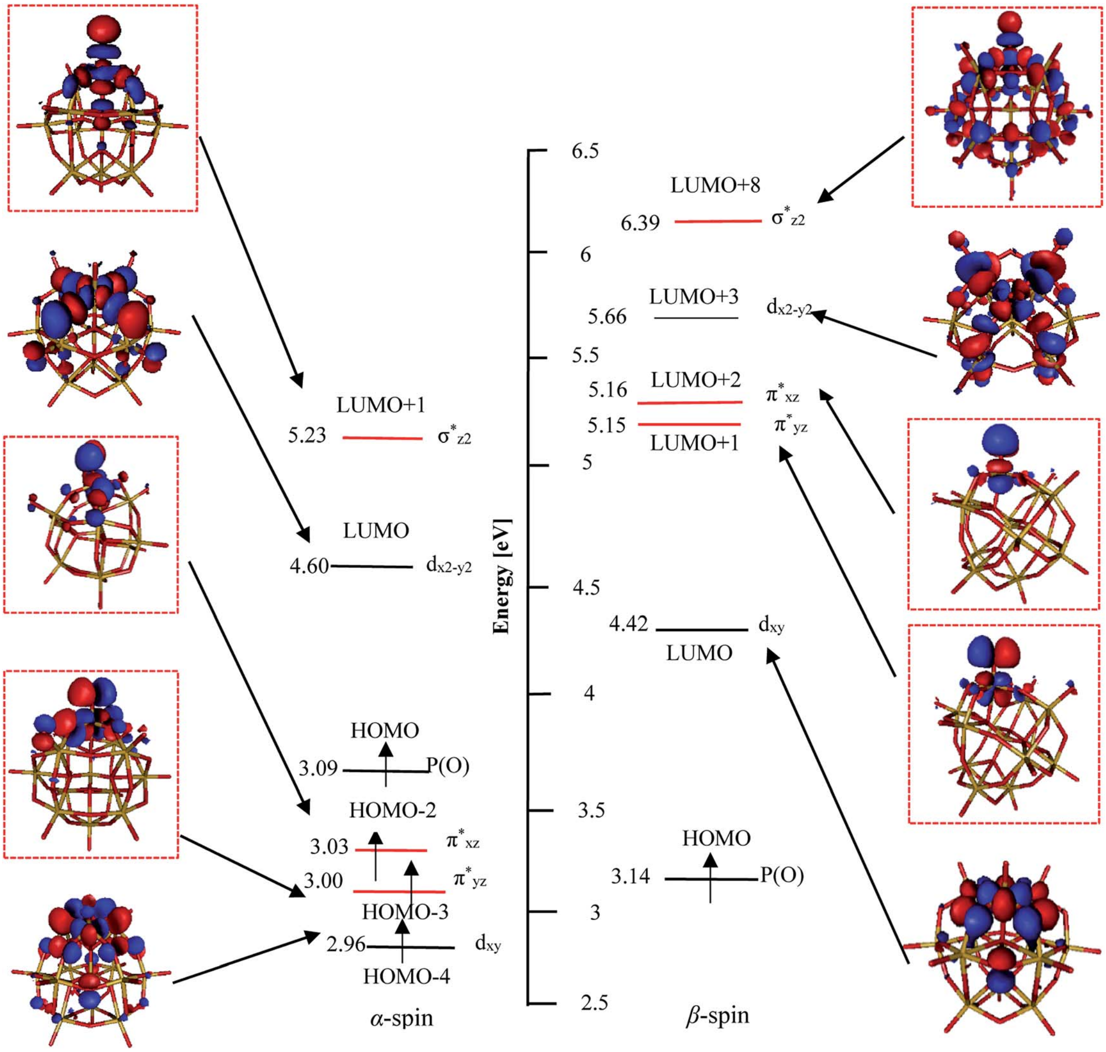

Fig. 5 The molecular orbitals expression of PWFe^{V}O calculated at UOPBE/6-31G(d) (LANL2DZ basis set on the metal atom) level. The orbital energy values have been represented in eV.

3. Computational details

All DFT computations of this work were performed with deMon2k program.[36] We used the OPTX exchange functional proposed by Cohen and Handy,[78,79] coupled with the Perdew–Becke–Ernzerhof (PBE) correlation functional.[80] This Generalized-Gradient-Approximation (GGA) functional has been shown adequacy for modeling iron–porphyrin and cobalt porphyrin complexes.[81–84] The Keggin type POM compounds were investigated by OPTX-PBE functional by assuming its adequacy based on previous studies.[26,34,85] The DFT energies and gradients were corrected by an empirical expression to indicate dispersion.[86] The Kohn–Sham equations were solved within the auxiliary DFT framework, where variationaly fitted auxiliary electron densities are applied in calculating both the Coulomb and the exchange-correlation (XC) potential.[87,88] An adaptive grid of fine mesh (tolerance 10^{-7} a.u.) was chosen for the numerical integration of the XC potential.[89] The basis set of DZVP-GGA (double-zeta-valence-polarization calibrated for generalized-gradient-approximation functional) on Fe, O, P, W and H was applied for geometry optimizations, frequency and electronic structure analyses.[90] The auxiliary electron density was expanded with the GEN-A2 auxiliary basis set on Fe, W, P, O and H.[91] The self-consistent-field iterations were run with convergence criteria of 10^{-8} hartree on the DFT energies. The geometry optimizations were performed with 1×10^{-5} hartree per bohr tolerance criteria on the energy gradients. No molecular symmetry was applied in geometry optimizations. Vibrational frequencies were obtained at the same level in this work. Cartesian coordinates of the optimized geometries of the complexes are presented in ESI.† Natural bond orbital (NBO) analysis at the OPBE/6-31G(d) level (LANL2DZ basis set on the metal atom)[92–94] was performed to assign the atomic charges, spin densities and effective bond order/Wiberg Bond Indices (WBI). The NBO calculations were done with the Gaussian 09 package,[95] considering only the ions without either counter cations or solvent molecules.

4 Conclusion

DFT/OPTX-PBE method has been employed to investigate the geometry, electronic structure, Fe–ligand bonding nature, and simulated IR spectrum of α-Keggin, lacunary Keggin, $Fe^{II/III}$ substituted and the important oxidized high-valent iron derivatives of Keggin type POMs. The most significant finding is briefed as follows:

(i) Increasing in the POM charge, like PW_{11}, results in no significant alteration of local charge at central PO_4^{3-}. This high charge density is accumulated in $W_{11}O_{35}$ framework of the POM and specially concentrated on the terminal oxygen atoms which increase their basicity.

(ii) The electronic structures provide basis for understanding the bonding interactions between Fe^{II} and POM ligand. Bonding MOs result from contribution of 3d atomic orbitals of Fe^{II} and 2p orbitals of oxygen in POM.

(iii) The simulated IR spectra show that four characteristic peaks of PW_{12} split into five owing to substitution of Fe atom in $PWFe^{n+}$ ($n = 2$ and 3).

(iv) The $PWFe^{II/III/IV}OH_2$ derivatives show the weak $Fe–O_{ligand}$ single bond and $PWFe^{IV/V/VI}O$ derivatives display the strong Fe═O double bond. So, it could be predicted that Fe oxidation state affect the antibonding interaction between Fe and ligand, which is the main character of these derivatives, and increase their activity in oxygen transfer processes.

(v) Relevant to other high-valent species, $PWFe^{V}O$ would be favourable for oxidation process because of low energy unoccupied π*-antibonding orbitals and high contribution of oxygen.

(vi) The FMO analysis indicated that Fe═O bonding interaction mainly comes from an effective overlapping between $2p_{x/y}$ orbitals of O^{2-} ligand and $3d_{xz/yz}$ orbitals of Fe, thus an electron transfer from oxygen to Fe atom could be occurred.

Conflicts of interest

There are no conflicts to declare.

Acknowledgements

The authors are thankful of University of Isfahan for financially support of this research. We are also grateful from Prof. Aurelien de La Lande (Laboratoire de Chimie Physique, LCP, CNRS) and the University of Paris-Sud for supporting our computations at Styx.

Notes and references

1 P. Gouzerh and A. Proust, *Chem. Rev.*, 1998, **98**, 77–112.
2 J. T. Rhule, C. L. Hill, D. A. Judd and R. F. Schinazi, *Chem. Rev.*, 1998, **98**, 327–358.
3 S.-S. Wang and G.-Y. Yang, *Chem. Rev.*, 2015, **115**, 4893–4962.
4 I. V. Kozhevnikov, *Chem. Rev.*, 1998, **98**, 171–198.
5 A. Proust, R. Thouvenot and P. Gouzerh, *Chem. Commun.*, 2008, 1837–1852.
6 T. Yamase, *Chem. Rev.*, 1998, **98**, 307–326.
7 M. Sono, M. P. Roach, E. D. Coulter and J. H. Dawson, *Chem. Rev.*, 1996, **96**, 2841–2888.
8 C. Wang, K. V. Shalyaev, M. Bonchio, T. Carofiglio and J. T. Groves, *Inorg. Chem.*, 2006, **45**, 4769–4782.
9 J. Kaizer, E. J. Klinker, N. Y. Oh, J. U. Rohde, W. J. Song, A. Stubna, J. Kim, E. Münck, W. Nam and L. Que, *J. Am. Chem. Soc.*, 2004, **126**, 472–473.
10 N. S. Antonova, J. J. Carbó, U. Kortz, O. A. Kholdeeva and J. M. Poblet, *J. Am. Chem. Soc.*, 2010, **132**, 7488–7497.
11 S. P. de Visser, D. Kumar, R. Neumann and S. Shaik, *Angew. Chem., Int. Ed.*, 2004, **43**, 5661–5665.
12 P. Jiménez-Lozano, I. Y. Skobelev, O. A. Kholdeeva, J. M. Poblet and J. J. Carbó, *Inorg. Chem.*, 2016, **55**, 6080–6084.
13 K. Kamata, T. Hirano, S. Kuzuya and N. Mizuno, *J. Am. Chem. Soc.*, 2009, **131**, 6997–7004.
14 K. Kamata, R. Ishimoto, T. Hirano, S. Kuzuya, K. Uehara and N. Mizuno, *Inorg. Chem.*, 2010, **49**, 2471–2478.
15 K. Kamata, Y. Nakagawa, K. Yamaguchi and N. Mizuno, *J. Am. Chem. Soc.*, 2008, **130**, 15304–15310.
16 A. E. Kuznetsov, Y. V. Geletii, C. L. Hill, K. Morokuma and D. G. Musaev, *Inorg. Chem.*, 2009, **48**, 1871–1878.
17 Z. L. Lang, G. C. Yang, M. N. Ma, S. Z. Wen, L. K. Yan, W. Guan and Z. M. Su, *Dalton Trans.*, 2013, **42**, 10617–10625.
18 C. G. Liu, W. Guan, L. K. Yan and Z. M. Su, *Eur. J. Inorg. Chem.*, 2011, 489–494.
19 C. G. Liu, W. Guan, L. K. Yan, P. Song and Z. M. Su, *Dalton Trans.*, 2009, 6208–6213.
20 C. G Liu, X. M. Jiang and Z. M. Su, *Inorg. Chem.*, 2017, **56**, 10496–10504.
21 J. M. Maestre, X. Lopez, C. Bo, J.-M. Poblet and N. Casan-Pastor, *J. Am. Chem. Soc.*, 2001, **123**, 3749–3758.
22 D. G. Musaev, K. Morokuma, Y. V. Geletii and C. L. Hill, *Inorg. Chem.*, 2004, **43**, 7702–7708.
23 Y. Nakagawa and N. Mizuno, *Inorg. Chem.*, 2007, **46**, 1727–1736.
24 R. Prabhakar, K. Morokuma, C. L. Hill and D. G. Musaev, *Inorg. Chem.*, 2006, **45**, 5703–5709.
25 J. Wang, C. Hu, M. Jian, J. Zhang and G. Li, *J. Catal.*, 2006, **240**, 23–30.
26 H. N. Wu, J. Wang, H. Li, N. N. Ma, T. Zhang, S. Q. Shi, L. K. Yan and Z. M. Su, *Comput. Theor. Chem.*, 2016, **1089**, 28–34.
27 M. X. Jiang and C. G. Liu, *J. Phys. Chem. C*, 2017, **121**, 12735–12744.
28 D. Quiñonero, Y. Wang, K. Morokuma, L. A. Khavrutskii, B. Botar, Y. V. Geletii, C. L. Hill and D. G. Musaev, *J. Phys. Chem. B*, 2006, **110**, 170–173.
29 Y. Wang, G. Zheng, K. Morokuma, Y. V. Geletii, C. L. Hill and D. G. Musaev, *J. Phys. Chem. B*, 2006, **110**, 5230–5237.
30 C.-G. Liu, S. Liu and T. Zheng, *Inorg. Chem.*, 2015, **54**, 7929–7935.
31 C. G. Liu, Z. M. Su, W. Guan and L. K. Yan, *Inorg. Chem.*, 2009, **48**, 541–548.
32 S. Romo, N. S. Antonova, J. J. Carbó and J. M. Poblet, *Dalton Trans.*, 2008, 5166–5172.

33 B. Zhu, Z. L. Lang, M. N. Ma, L. K. Yan and Z. M. Su, *Phys. Chem. Chem. Phys.*, 2014, **16**, 18017–18022.
34 E. Derat, D. Kumar, R. Neumann and S. Shaik, *Inorg. Chem.*, 2006, **45**, 8655–8663.
35 W. Guan, L. Yan, Z. Su, S. Liu, M. Zhang and X. Wang, *Inorg. Chem.*, 2005, **44**, 100–107.
36 A. Koster, G. Geudtner, P. Calaminici, M. Casida, V. Dominguez, R. Flores-Moreno, G. Gamboa, A. Goursot, T. Heine and A. Ipatov, *DeMon2k, Version 3, The deMon Developers*, Cinvestav, Mexico City, Mexico, 2011.
37 R. Neumann and A. M. Khenkin, *J. Mol. Catal. A: Chem.*, 1996, **114**, 169–180.
38 P. Souchay, *Polyanions et polycations*, Gauthier-Villars, 1963.
39 X. Lo'pez, J. J. Carbo', C. Bo and J. M. Poblet, *Chem. Soc. Rev.*, 2012, **41**, 7537–7571.
40 B. Courcot and A. J. Bridgeman, *Int. J. Quantum Chem.*, 2010, **110**, 2155–2161.
41 B. Courcot and A. J. Bridgeman, *J. Comput. Chem.*, 2011, **32**, 240–247.
42 B. Courcot and A. J. Bridgeman, *J. Comput. Chem.*, 2011, **32**, 1703–1710.
43 B. Courcot and A. J. Bridgeman, *J. Comput. Chem.*, 2011, **32**, 3143–3153.
44 M. R. Farsani and B. Yadollahi, *J. Mol. Catal. A: Chem.*, 2014, **392**, 8–15.
45 I. Böschen, B. Buss and B. Krebs, *Acta Crystallogr., Sect. B: Struct. Crystallogr. Cryst. Chem.*, 1974, **30**, 48–56.
46 C. L. Hill and R. B. Brown, *J. Am. Chem. Soc.*, 1986, **108**, 536–538.
47 M. Colladon, A. Scarso, P. Sgarbossa, R. A. Michelin and G. Strukul, *J. Am. Chem. Soc.*, 2007, **129**, 7680–7689.
48 N. Mizuno and M. Misono, *Chem. Rev.*, 1998, **98**, 199–218.
49 N. Mizuno, K. Yamaguchi and K. Kamata, *Coord. Chem. Rev.*, 2005, **249**, 1944–1956.
50 Y. Sawada, K. Matsumoto and T. Katsuki, *Angew. Chem., Int. Ed.*, 2007, **46**, 4559–4561.
51 D. Mansuy, J. F. Bartoli, P. Battioni, D. K. Lyon and R. G. Finke, *J. Am. Chem. Soc.*, 1991, **113**, 7222–7226.
52 T. A. Betley and J. C. Peters, *J. Am. Chem. Soc.*, 2004, **126**, 6252–6254.
53 M. D. Fryzuk, S. A. Johnson, B. O. Patrick, A. Albinati, S. A. Mason and T. F. Koetzle, *J. Am. Chem. Soc.*, 2001, **123**, 3960–3973.
54 A. Hiskia and E. Papaconstantinou, *Inorg. Chem.*, 1992, **31**, 163–167.
55 L. Eberson, *New J. Chem.*, 1992, **16**, 151–156.
56 I. A. Weinstock, *Chem. Rev.*, 1998, **98**, 113–170.
57 R. Tonner, F. Öxler, B. Neumüller, W. Petz and G. Frenking, *Angew. Chem., Int. Ed.*, 2006, **45**, 8038–8042.
58 H. Chen, M. Ikeda-Saito and S. Shaik, *J. Am. Chem. Soc.*, 2008, **130**, 14778–14790.
59 F. M. Santos, S. P. Magina, H. I. Nogueira and A. M. Cavaleiro, *New J. Chem.*, 2016, **40**, 945–953.
60 S. Afewerki and A. Cordova, *Chem. Rev.*, 2016, **116**, 13512–13570.
61 F. G. Gelalcha, *Chem. Rev.*, 2007, **107**, 3338–3361.
62 T. Mallat and A. Baiker, *Chem. Rev.*, 2004, **104**, 3037–3058.
63 V. C. C. Wang, S. Maji, P. P. Y. Chen, H. K. Lee, S. S. F. Yu and S. I. J. C. R. Chan, *Chem. Rev.*, 2017, **117**, 8574–8621.
64 B. Zhang, H. Asakura, J. Zhang, J. Zhang, S. De and N. Yan, *Angew. Chem., Int. Ed.*, 2016, **55**, 8319–8323.
65 C. L. Hill and C. M. Prosser-McCartha, *Coord. Chem. Rev.*, 1995, **143**, 407–455.
66 J. Roithova and D. Schroder, *Chem. Rev.*, 2009, **110**, 1170–1211.
67 S. Shaik, H. Hirao and D. Kumar, *Acc. Chem. Res.*, 2007, **40**, 532–542.
68 S. Shaik, D. Kumar, S. P. de Visser, A. Altun and W. Thiel, *Chem. Rev.*, 2005, **105**, 2279–2328.
69 R. Neumann and C. Abu-Gnim, *J. Am. Chem. Soc.*, 1990, **112**, 6025–6031.
70 C. Rong and M. T. Pope, *J. Am. Chem. Soc.*, 1992, **114**, 2932–2938.
71 M. T. Pope and A. Müller, *Angew. Chem., Int. Ed.*, 1991, **30**, 34–48.
72 M. Sadakane and E. Steckhan, *Chem. Rev.*, 1998, **98**, 219–238.
73 A. Decker, M. S. Chow, J. N. Kemsley, N. Lehnert and E. I. Solomon, *J. Am. Chem. Soc.*, 2006, **128**, 4719–4733.
74 A. Decker, J.-U. Rohde, L. Que and E. I. Solomon, *J. Am. Chem. Soc.*, 2004, **126**, 5378–5379.
75 J. A. Fernández, X. López, C. Bo, C. de Graaf, E. J. Baerends and J. M. Poblet, *J. Am. Chem. Soc.*, 2007, **129**, 12244–12253.
76 X. López, J. A. Fernández and J. M. Poblet, *Dalton Trans.*, 2006, 1162–1167.
77 S. Romo, J. A. Fernández, J. M. Maestre, B. Keita, L. Nadjo, C. de Graaf and J. M. Poblet, *Inorg. Chem.*, 2007, **46**, 4022–4027.
78 N. C. Handy and A. J. Cohen, *Mol. Phys.*, 2001, **99**, 403–412.
79 M. Swart, A. W. Ehlers and K. Lammertsma, *Mol. Phys.*, 2004, **102**, 2467–2474.
80 J. P. Perdew, K. Burke and M. Ernzerhof, *Phys. Rev. Lett.*, 1996, **77**, 3865.
81 A. de la Lande, M.-H. Ha-Thi, S. Chen, B. Soep and N. Shafizadeh, *Phys. Chem. Chem. Phys.*, 2016, **18**, 16700–16708.
82 M. M. Conradie, J. Conradie and A. Ghosh, *J. Inorg. Biochem.*, 2011, **105**, 84–91.
83 M. Aarabi, R. Omidyan, S. Soorkia, G. Grégoire, M. Broquier, M.-E. Crestoni, A. de La Lande, B. Soep and N. Shafizadeh, *Phys. Chem. Chem. Phys.*, 2019, **21**, 1750–1760.
84 M. Aarabi, S. Soorkia, G. Grégoire, M. Broquier, A. de la Lande, B. Soep, R. Omidyan and N. Shafizadeh, *Phys. Chem. Chem. Phys.*, 2019, **21**, 21329–21340.
85 C. G. Liu, *Mol. Phys.*, 2011, **109**, 1851–1857.
86 A. Goursot, T. Mineva, R. Kevorkyants and D. Talbi, *J. Chem. Theory Comput.*, 2007, **3**, 755–763.
87 R. Flores-Moreno and A. M. Köster, *J. Chem. Phys.*, 2008, **128**, 134105.
88 A. Vela, V. Medel and S. Trickey, *J. Chem. Phys.*, 2009, **130**, 244103.
89 M. Krack and A. M. Köster, *J. Chem. Phys.*, 1998, **108**, 3226–3234.
90 P. Calaminici, F. Janetzko, A. M. Köster, R. Mejia-Olvera and B. Zuniga-Gutierrez, *J. Chem. Phys.*, 2007, **126**, 044108.

91 T. Clark, J. Chandrasekhar, G. W. Spitznagel and P. V. R. Schleyer, *J. Comput. Chem.*, 1983, **4**, 294–301.

92 P. J. Hay and W. R. Wadt, *J. Chem. Phys.*, 1985, **82**, 270–283.

93 P. J. Hay and W. R. Wadt, *J. Chem. Phys.*, 1985, **82**, 299–310.

94 W. R. Wadt and P. J. Hay, *J. Chem. Phys.*, 1985, **82**, 284–298.

95 M. J. Frisch, G. W. Trucks, H. B. Schlegel, G. E. Scuseria, M. A. Robb, J. R. Cheeseman, G. Scalmani, V. Barone, G. A. Petersson, H. Nakatsuji, X. Li, M. Caricato, A. Marenich, J. Bloino, B. G. Janesko, R. Gomperts, B. Mennucci, H. P. Hratchian, J. V. Ortiz, A. F. Izmaylov, J. L. Sonnenberg, D. Williams-Young, F. Ding, F. Lipparini, F. Egidi, J. Goings, B. Peng, A. Petrone, T. Henderson, D. Ranasinghe, V. G. Zakrzewski, J. Gao, N. Rega, G. Zheng, W. Liang, M. Hada, M. Ehara, K. Toyota, R. Fukuda, J. Hasegawa, M. Ishida, T. Nakajima, Y. Honda, O. Kitao, H. Nakai, T. Vreven, K. Throssell, J. J. A. Montgomery, J. E. Peralta, F. Ogliaro, M. Bearpark, J. J. Heyd, E. Brothers, K. N. Kudin, V. N. Staroverov, T. Keith, R. Kobayashi, J. Normand, K. Raghavachari, A. Rendell, J. C. Burant, S. S. Iyengar, J. Tomasi, M. Cossi, J. M. Millam, M. Klene, C. Adamo, R. Cammi, J. W. Ochterski, R. L. Martin, K. Morokuma, O. Farkas, J. B. Foresman and D. J. Fox, *Gaussian 09*, Gaussian, Inc., Wallingford CT, 2013.